

Detecting Infrared Single Photons with Near-Unity System Detection Efficiency

J. Chang^{1,2,†}, J. W. N. Los^{2,†}, J. O. Tenorio-Pearl², N. Noordzij², R. Gourgues², A. Guardiani², J. R. Zichi³, S. F. Pereira¹, H. P. Urbach¹, V. Zwiller^{2,3}, S. N. Dorenbos², and I. Esmaeil Zadeh^{1,2}

¹Optics Research Group, ImPhys Department, Faculty of Applied Sciences, Delft University of Technology, Delft 2628 CJ, The Netherlands.

²Single Quantum B.V., Delft 2628 CJ, The Netherlands.

³KTH Royal Institute of Technology, Department of Applied Physics, Albanova University Centre, Roslagstullsbacken 21, 106 91 Stockholm, Sweden

*Corresponding author: j.chang-1@tudelft.nl

† These authors contributed equally to this work.

ABSTRACT

Single photon detectors are indispensable tools in optics, from fundamental measurements to quantum information processing. The ability of superconducting nanowire single photon detectors to detect single photons with unprecedented efficiency, short dead time and high time resolution over a large frequency range enabled major advances in quantum optics. However, combining near-unity system detection efficiency with high timing performance remains an outstanding challenge. In this work, we show novel superconducting nanowire single photon detectors fabricated on membranes with 94-99.5 ($\pm 2.07\%$) system detection efficiency in the wavelength range 1280-1500 nm. The SiO_2/Au membrane enables broadband absorption in small SNSPDs, offering high detection efficiency in combination with high timing performance. With low noise cryogenic amplifiers operated in the same cryostat, our efficient detectors reach timing jitter in the range of 15-26 ps. We discuss the prime challenges in optical design, device fabrication as well as accurate and reliable detection efficiency measurements to achieve high performance single-photon detection. As a result, the fast developing fields of quantum information science, quantum metrology, infrared imaging and quantum networks will greatly benefit from this far-reaching quantum detection technology.

Introduction

Superconducting nanowire single photon detectors (SNSPDs) emerged as a key enabling technology for quantum optics experiments and photonics applications over the last two decades¹⁻³. Achieving unity system detection efficiency (SDE) with SNSPDs has been a long-standing, yet very challenging goal. For example, in quantum key distribution (QKD) systems⁴⁻⁶, single photon detectors with high efficiency are essential for receiving secured quantum keys over long distances. High efficiency detectors also allow closing loopholes and certify that a quantum communication scheme based on entanglement is secure⁷. Also, for experiments requiring coincidence measurements in multiple detectors, near-unity detection efficiency is required for each channel because the multi photon count rate depends on the efficiency product of detectors involved. For example, the 12-photon coincidence count rate⁸ is about one per hour with 75% efficiency detectors. For the same measurement, if 99.5% efficiency detectors could be used, the coincidence count rate would be increased to one per two minutes. Similarly, in Boson sampling, single photon detectors with high SDE are required in ambitious experiments aiming for quantum supremacy⁹. Besides near-unity system efficiency, high timing performance is crucial for applications where photon arrival time is required to be precisely recorded. For example, in high-dimensional QKD^{10,11}, multiple bits per photon pair can be realized by encoding information in the photons' arrival times, high efficiency and time resolution are thus both required. Similarly, high timing performance is essential for improving depth resolution in light detection and ranging^{12,13}, distinguishing signal from false counts in dark matter detection¹⁴, enhancing the quality of quantum imaging systems^{15,16} as well as making photons with small energy difference indistinguishable for quantum erasure application¹⁷. More radically, the fast-expanding quantum technologies in recent years are based on quantum states that violate local realism, as shown in^{18,19}, high performance SNSPDs have played important roles in experiments that successfully demonstrated loophole-free violation of Bell's inequalities.

With demands from emerging applications as well as the quest to understand SNSPDs' detection limits, efforts were made in the past years to improve SDE towards unity²⁰⁻²⁵. As summarized in table 1, different material platforms were developed to achieve the highest SDE. However, achieving unity efficiency simultaneously with ultrahigh time resolution remains a

challenge. Here, using a relatively thick NbTiN superconducting film and membrane cavity, we demonstrate SNSPDs with over 99% SDE at 1350 nm (also over 98% SDE at 1425 nm, see [Supplementary Material](#) section "List of measured devices") and above 94% efficiency in the wavelength range 1280-1500 nm. These detectors also achieved 15-26 ps timing jitter with cryogenic amplification readout circuitry and an electrical recovery time of about 33 ns (1/e recovery time). Additionally, we clarify explicitly SNSPDs' efficiency measurement pitfalls and requirements, which will be a solid reference for single photon applications and characterization of single photon detectors.

Table 1. Comparison of different high efficiency SNSPDs works

Material/ Temperature	SDE/ Jitter	Wavelength	Reference
WSi/120 mK	93%/150 ps	1550 nm	ref. ²⁰
NbN/1.8-2.1 K	90-92%/79 ps	1550 nm	ref. ²¹
NbTiN/2.5 K	92%/14.8 ps	1310 nm	ref. ²²
MoSi/700 mK	95%/unknown	1520-1550 nm	ref. ²³
MoSi/700 mK	98%/unknown	1550 nm	ref. ²⁴
NbN/800 mK-2.1 K	95-98%/65.8-106 ps	1530-1630 nm	ref. ²⁵
NbTiN/2.5 K	94-99.5%/15.1 ps	1290-1500 nm	This work

Optical Simulation and Device Design

Typically, SNSPDs are meandering superconducting nanowires embedded in an optical cavity. An optimized optical cavity and meandered nanowire design are indispensable to achieve high system detection efficiency. Recent results^{23,24} showed that SNSPDs integrated with distributed Bragg reflectors (DBR) enable high system detection efficiency. However, since light is reflected several times in the cavity before being completely absorbed, the beam diverges and bigger detectors were made at the cost of longer recovery times (dead time in the order of few hundred nanoseconds) to have good absorption. Also, fabrication of large detectors inevitably increases the timing jitter of the detectors. More complex double-layer meanders were also reported to achieve high absorption and thus high SDE²⁵. However, the additional meander layer increases fabrication complexity and large active areas are still needed to have strong absorption. In this work, we employ a different approach: a meandering superconducting nanowire is fabricated on a thin SiO_2 membrane with a Au reflector underneath. We made two different meandered nanowire designs: 50/120 nm and 70/140 nm (line-width/pitch). Both designs have a radius of 8 μm so that our device diameter is 30-70% smaller than recent reported high SDE works^{24,25}. The top panel in figure 1 (a) illustrates the NbTiN nanowire supported by SiO_2 /Au membrane and bottom panel shows an optical microscope image of the meandered nanowire on SiO_2 membrane before (left) and after (right) deposition of Au reflector. This compact optical cavity design allows us to make smaller meandering nanowires without degrading the SDE. Also, a smaller device leads to lower kinetic inductance, translating into a faster detection signal rising edge and better timing performance.²⁶⁻²⁸

To achieve efficient optical fiber to detector coupling, we used the ferule-sleeve method described in²². The air gap between detector and fiber plays an important role in the total optical absorption. The air gap is defined by multiple sources: (i) fabrication residuals left around the device or dust on the fiber end surface, (ii) Au contacts around the detector, (iii) potential drift of fiber core during cooling/warming, leaving a gap between detector and fiber. In this work, Finite-difference time-domain (FDTD) simulations were carried out for a systematic study of the optical absorption. As shown in figure 1 (b), when the air gap is around 2.2 μm , only one efficiency peak can be observed along cutline 1. As a result, figure 1 (c) shows simulation and measurement results of detector #1 with >99% SDE at 1350 nm. With the increase of the air gap distance, more complex absorption situations are obtained. For example, along cutline 2, dual absorption peaks are expected. We point out that an air gap doesn't always reduce absorption. With proper control of the air gap, one could achieve maximum absorption at selected wavelengths. As a direct demonstration, figure 1 (d) shows simulation and measurements of detector #2 with two SDE peaks: at 1280 nm and at 1500 nm. Both SDEs exceed 94% similar to previously reported more complex cavities²⁹ and controlled design of such detectors would benefit applications where multiple wavelengths must be efficiently detected simultaneously.

Device Fabrication

Based on simulation results, device fabrication was carried out as described below. Initially, a 230 nm thick SiO_2 layer was grown by thermal oxidation on a commercial Si wafer. On top of the SiO_2 , a NbTiN thin film was deposited by co-sputtering of Nb and Ti in a plasma of Ar and N_2 as described in³⁰. The meandering nanowire structure was then written by electron beam lithography with either HSQ (1st batch, negative) or ARP-62009 (2nd batch, positive) E-beam resist. After development,

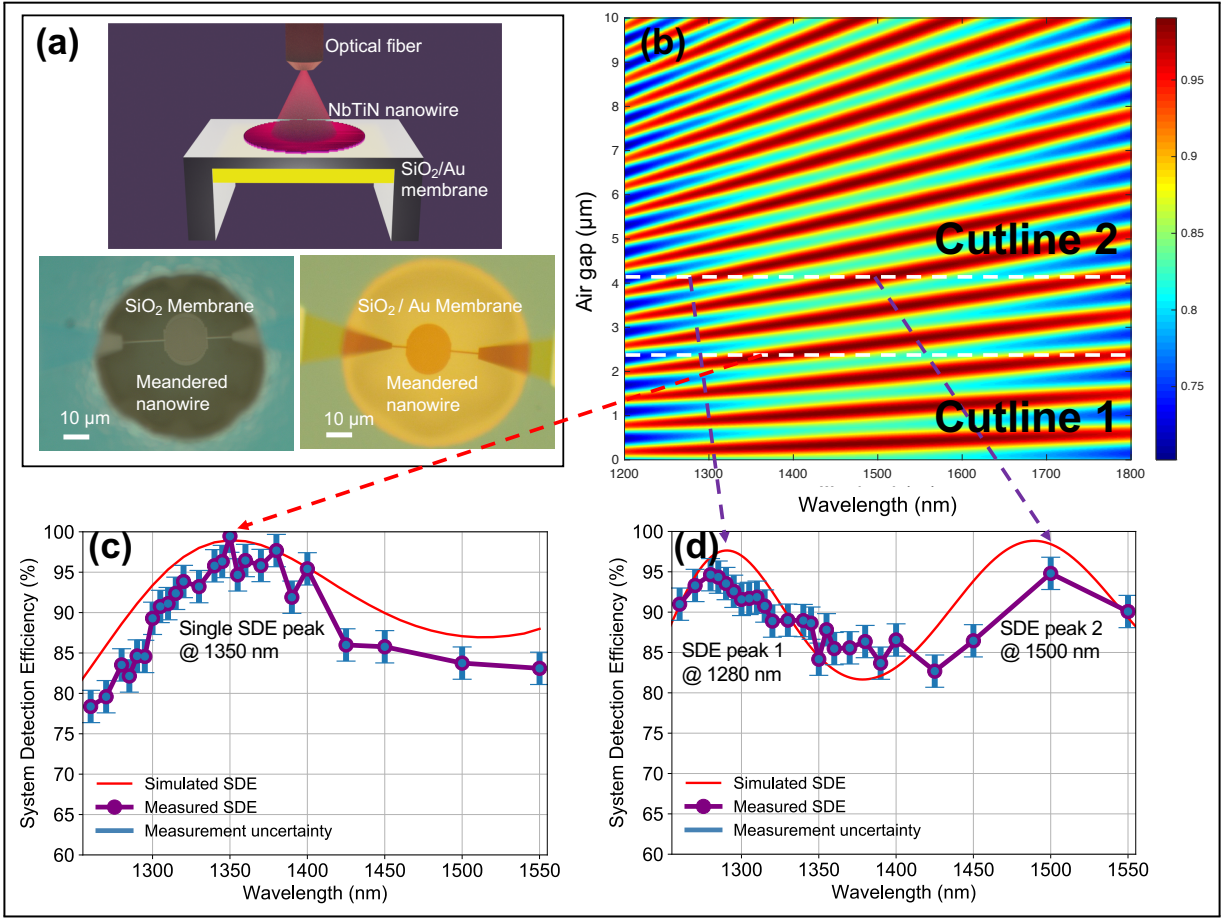


Figure 1. (a) Top panel illustrates the device structure of meandered nanowire on SiO_2/Au membrane and bottom panel shows optical image of the meandered nanowire on SiO_2 membrane before/after (left/right) Au deposition. (b) Simulated optical absorption for a device with 0-10 μm air gap. Cutline 1 shows when the air gap is around 2.2 μm , only one SDE peak occurs around 1350 nm and cutline 2 shows that with an air gap of 4.1 μm , two SDE peaks are obtained. (c) Measurement and simulation of detector #1 with SDE over 99% at 1350 nm. (d) Measurement and simulation of detector #2 with dual peaks at 1280 nm and 1500 nm, both exceeding 94% SDE.

the nanowire pattern was transferred to the NbTiN layer by reactive ion etching with mixed gases of SF_6 and O_2 . Afterwards, using deep reactive ion etching and metal evaporation, we fabricated a thin SiO_2 membrane with a Au mirror beneath the NbTiN nanowire as described in [Supplementary Material](#) section "Device Fabrication". Finally, a deep Silicon etch step (Bosch etching) released the detectors.

Efficiency Measurement Setup

Prior to any measurement, the laser was turned on for > 1 hour for power stabilization. Every optical component including fibers were fixed to avoid influence from mechanical vibration and air turbulence. We used the following two-step procedure to carry out system efficiency measurements: (i) Building an accurate laser attenuator. Initially, the continuous-wave (CW) laser beam passes through the first fiber-to-fiber coupler (FBC-1550-FC, containing a polarizer) followed by a fiber-coupled beam splitter (with a splitting ratio of 99-1). The high power branch is recorded by an optical power meter P_1 while the low power branch is directed towards the second fiber-to-fiber coupler (containing neutral density filters and a polarizer) and a polarization controller. Similarly, the power after the polarization controller is recorded with an optical power meter P_2 . By adjusting polarizers in both fiber-to-fiber couplers and choosing the proper neutral density filters, we set the power ratio P_1/P_2 to the desired values (50-60 dB). After the attenuation ratio was set, all components were kept fixed. (ii) Controlling precisely the input photon flux. We lowered the input power by adding extra neutral density filters before passing through the first polarizer to lower P_1 to 1-10 nW. We also rechecked the attenuation ratio multiple times before and after the measurements to assure nothing has been changed in the setup (see [Supplementary Material](#) section "Efficiency measurement stability"). After this

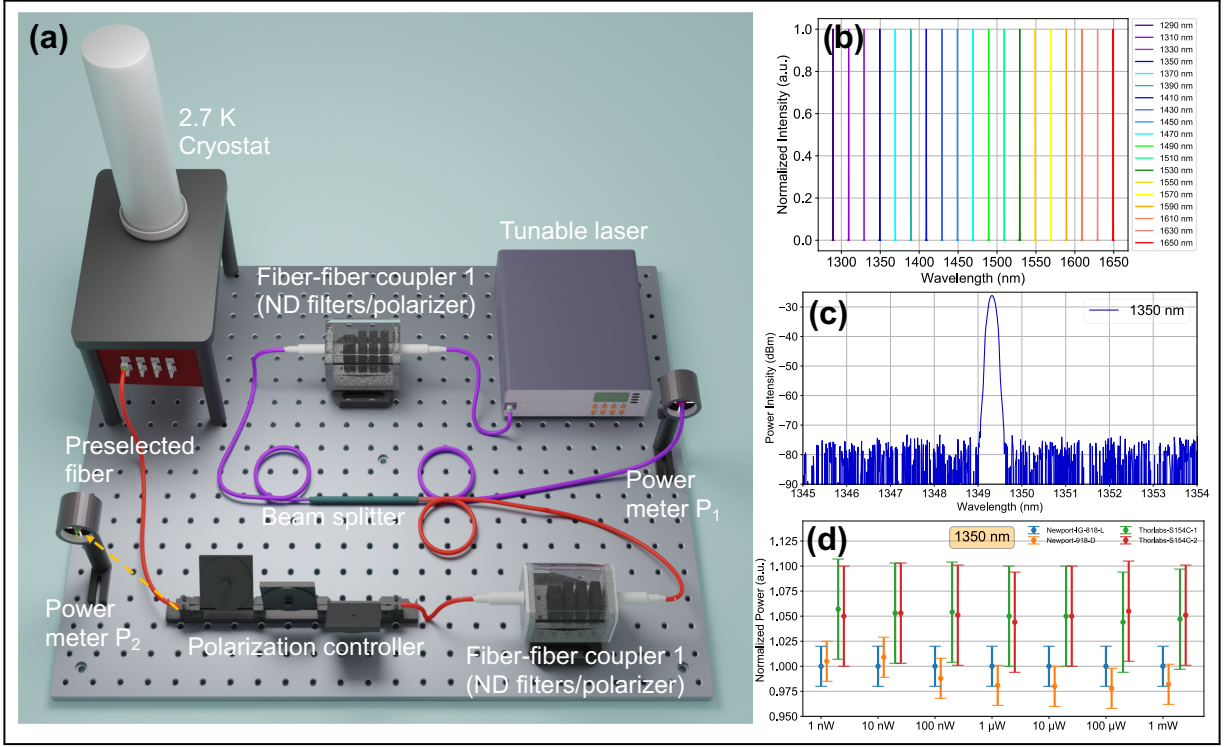


Figure 2. (a) System detection efficiency measurement setup. Emission from a tunable laser passes a bench containing neutral density (ND) filters and a polarizer, and goes through a 99-1 fiber-coupled beam splitter to split the signal towards power meter P_1 (99%) and power meter P_2 (1%). (b) Measured spectrum of the tunable laser at 1290-1650 nm. (c) Measured laser spectrum at 1350 nm shows a laser linewidth of < 1 nm. (d) Four different optical power meters' readings at 1350 nm with different error bars. All readings are normalized to the Newport IG-818-L power meter.

two-step procedure, different input photon fluxes can be set up, for example 10 nW with 50 dB attenuation corresponds to 679k photons per second at 1350 nm. It must be noted that, to avoid fiber-to-fiber coupling losses when connecting to the detection system, we preselected the fibers which have the best coupling match to the fibers inside our cryostat. Finally, the fiber at the output of the polarization controller was connected to the preselected fiber and then guide light into the system for measurements.

Our SDE was calculated as $\eta_{SDE} = (1 - R_{rfl}) \cdot (N_{count}/N_{total})$, where N_{count} is the total registered count rate by our system and N_{total} is the total input photon number. R_{rfl} is added to avoid overestimation of the SDE and it represents the simulated and measured fiber-air interface reflection (see [Supplementary Material](#) section "Fiber end-face reflection"). Since the total input photon flux was calculated by $N_{total} = P \cdot \lambda / (hc)$, where P is the measured optical power, h is plank constant, c is the speed of light in vacuum and λ is the used wavelength, we carefully evaluate our laser spectrum with an optical spectrum analyzer. In figure 2 (b), we show the measured spectrum of the tunable laser at variable wavelengths, from 1290 to 1650 nm. As a result, figure 2 (c) demonstrates that the laser has a linewidth of < 1 nm. The slight shift of the measured wavelength with the set value is mainly due to the optical spectrum analyzer's calibration off, which has negligible influence on our SDE measurement. For input power measurement, accurate optical power meters are necessary. As shown in 2 (d), four different optical power meters' readings at 1350 nm are presented with their uncertainties. All readings are normalized to the Newport IG-818-L (used for our measurements) since it has 2% accuracy from 20 pW until 10 mW and a good linearity uncertainty of 0.5%.

Detection performance and Discussion

Prior to SDE measurements, we studied the relationship between SNSPDs detection reset kinetics and their efficiency recovery. We performed auto-correlation measurements between two subsequent detection events with the detectors illuminated by a CW laser similar to³¹. After collecting more than 50 thousand events, as shown on the top panel of figure 3 (a), we built a delay time histogram. Together with the SNSPD detection pulse shown at the bottom panel of 3 (a), we can see that within the first 25 ns, no subsequent pulse can be detected thus $\tau_1 = 25$ ns can be defined as the minimum separation dead time. For most SNSPD related studies, $1/e$ dead time (time for pulse to decay from peak amplitude to $1/e$ of the amplitude) is often used to describe the

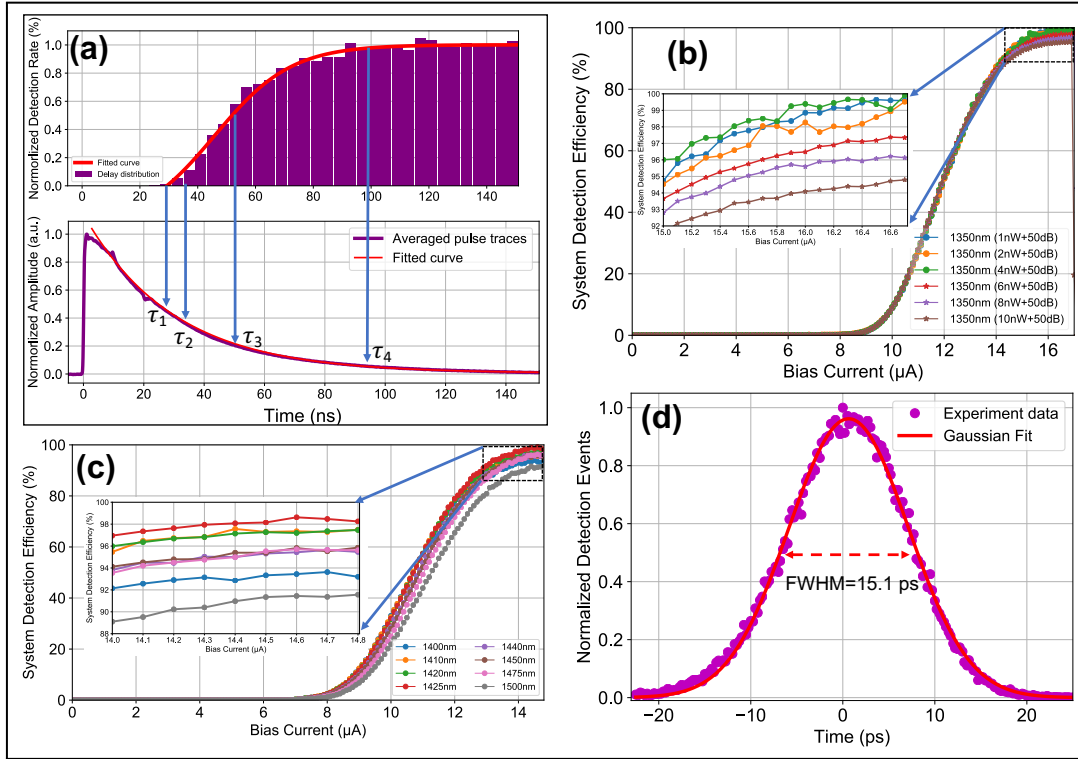


Figure 3. (a) The top inset shows the auto-correlation measurement of a detector indicating SDE recovery dynamics. The bottom inset shows an averaged pulse trace from the same detector. (b) SDE measurements of detector #1 at 1350 nm with different input photon fluxes. When input photon flux is below 4 nW plus 50 dB attenuation, the SDE of detector #2 reached >99%, which is also shown in the inserted picture. (c) SDE measurements of detector #3 at different wavelengths. The maximum SDE of detector #3 reached >98% at 1425 nm. (d) Jitter measurement from a detector with > 91% SDE with cryogenic amplifier. A Gaussian fit gives a FWHM jitter of 15.1 ps.

device recovery property. It can be seen that our device's $1/e$ dead time is $\tau_2=33$ ns. Furthermore, $\tau_3=51$ ns represents the time when the detector recovers 50% of the maximum efficiency, also known as -3dB efficiency dead time and $\tau_4=97$ ns stands for full efficiency recovery time. These measurements indicate that input photon flux can influence SDE because if the photon flux is too high, photons arriving within the dead times of the detector can not be registered at the detectors' maximum efficiency, thus optimal input photon flux is necessary to achieve maximum detection efficiency. It must be noted that much higher photon fluxes can be achieved (with no loss of efficiency) if the source is pulsed (photons arriving with regular timings in between)²².

We characterized 40 detectors in two separate fabrication rounds. As shown in figure 3 (b), detector #1 was the best detector from the first fabrication batch and was tested at 1350 nm with different input photon flux. Initially, the photon flux was set to 10 nW plus 50 dB attenuation ($\sim 679,000$ photons/s), and device #1 showed SDE of 94-95%. With an input photon flux below 4 nW plus 50 dB attenuation ($\sim 271,600$ photons/s), device #1 achieved saturated SDE of >99%. Similarly, detector #3 from the second fabrication batch was tested at different wavelengths and showed >98% SDE at 1425 nm as shown in figure 3 (c). For more examples, see [Supplementary Material](#) section "List of measured devices".

Besides high SDE, time resolution is another crucial advantage of SNSPDs compared with other single photon detectors. The Instrument Response Function (IRF) of our detectors were characterized with a ps-pulse laser (1064 nm) and a fast oscilloscope (4 GHz bandwidth, 40 GHz sampling rate) as described in²². As shown in 3 (d), with a low-noise cryogenic amplifier mounted at 40 K stage in the same cryostat, the IRF of device #15 shows a Gaussian shape histogram, after fitting we obtain 15.1 ± 0.05 ps (full width at half maximum, FWHM) timing jitter. This detector was measured to have more than 91% SDE and the ultra low timing jitter was mainly achieved by fabricating relatively small detectors, which results in lower kinetic inductance and thus better jitter^{27,28}. For more statistics of jitter measurement, see [Supplementary Material](#) section "Overview of tested detectors". In short we achieved 15.1-26 ps jitter with cryogenic amplifier and 29-39 ps jitter with room-temperature amplifiers readout circuitry.

Conclusion

In conclusion, we demonstrated NbTiN based SNSPDs operated at 2.7K with over 94% system efficiency in the wavelength range 1280-1500 nm with the highest system efficiency of $99.5 \pm 2.07\%$. At the same time, our detectors showed timing jitter in the range 15.1-26 ps with cryogenic amplifiers. The ultrahigh efficiencies were achieved using the following methods: (i) optimized thick NbTiN superconducting film with saturated internal efficiency, (ii) optimized broadband membrane cavity coupled to small detectors, and (iii) accurate system efficiency measurements with a narrow linewidth tunable laser to precisely locate the high-efficiency peaks. Compared with previous reported high-efficiency SNSPDs^{20,23,24}, our work presents a platform with higher operation temperature (2.7 K, compatible with compact closed-cycle cryostats), short recovery time, and high timing resolution. At the same time, the system efficiency performance of our devices are in par with recently reported NbN based SNSPDs²⁵ but using simpler fabrication (single-layer meander), higher operation temperature (no need for mK cooler), and better timing resolution. Our detectors can be further developed by considering the following aspects: (i) multiplexing detector and control individual pixels by cryo-CMOS electronics to realize imaging at the single photon level (ii) extending the detection spectrum in the mid-infrared by tailoring and optimizing NbTiN films and (iii) improving working temperature of the detectors with novel superconducting materials.

Methods

To achieve accurate SNSPD efficiency measurements, we addressed the following aspects separately.

Optical Simulation

To simulate the absorption of the optical stack, we used the commercially available FDTD Solutions software from Lumerical. The SNSPD was modeled as the cross-section of a single nanowire in an optical cavity. From top to bottom, the simulated stack structure was: optical fiber layer (SiO_2), airgap, NbTiN meander, $1/4 \lambda$ SiO_2 layer, and a 200 nm thick Au mirror. For more details about simulation settings and parameters, see [Supplementary Material](#) section "Optical Simulation".

Laser Source

A tunable laser (JGR-TLS5) with attenuation was employed as a quasi single photon source. The laser covers the range 1260-1650 nm with a step size of 0.1 nm (FWHM). For more details on the laser, see [Supplementary Material](#) section "Tunable laser source". Compared with previous work²² which used photodiodes operated at a single wavelength, the tunable laser has two major advantages: First, its narrow spectrum (<1 nm) at a tuned frequency allows for precise measurements; Second, a laser with tunable wavelength enabled mapping system efficiency at different wavelengths. In this way we precisely determine peak efficiency and built the spectral response.

Optical Power Meters

A semiconductor-based optical power meter was the key reference for efficiency measurements. In this work, we used two different types of power meters: Thorlabs S154C (NIST traceable, $\pm 5\%$ uncertainty), Newport 818-IG-L (NIST traceable, $\pm 2\%$ uncertainty). However, for the measurement, one should not only take the power meter accuracy into consideration, but also consider sensor linearity, spectral range, power range, stability and all other related parameters. For details, see [Supplementary Material](#) section "Optical power meters".

Measurement Uncertainty Calculation

For system detection efficiency measurement uncertainty, we considered all possible uncertainties in our experiments and calculated the total measurement uncertainty with the root-mean-square (RMS) of the sum of the squared errors. The uncertainties in our measurements include the power meter measurement uncertainty (2%) and linearity uncertainty (0.5%), laser stability uncertainty ($<0.1\%$) and optical attenuator uncertainty ($<0.2\%$). For detailed measurement uncertainty calculations, see [Supplementary Material](#) section "Efficiency measurement stability" and "Measurement uncertainty". In short, our efficiency measurement has a total uncertainty of $\pm 2.07\%$ (RMS).

Fiber end-face reflection

When measuring laser power within the fiber with a power meter, the fiber end-facet was not in direct contact with the power meter's sensor. The existing fiber-to-air interface leads to a reflection up to a few percent back towards the light source.²² On the other hand, Physical Contact polished fiber to fiber connections have negligible back reflections (typically -30 to -40 dB). For all our efficiency measurements, we removed this back reflection contribution by multiplying a correction factor of $(1-R_{rfl})$. To determine the accurate value of R_{rfl} , see [Supplementary Material](#) section "Fiber end-face reflection".

Polarization Degree

Since our detectors were patterned along meandering shapes, light absorption can be significantly different based on the light polarization direction along the meander's direction³². Thus it is important to have a linearly polarized input light and fully control the polarization. In [Supplementary Material](#) section "Polarization degree and control" we show detailed measurement of degree of linearity and polarization control.

References

1. Gol'Tsman, G. *et al.* Picosecond superconducting single-photon optical detector. *Appl. physics letters* **79**, 705–707 (2001).
2. Natarajan, C. M., Tanner, M. G. & Hadfield, R. H. Superconducting nanowire single-photon detectors: physics and applications. *Supercond. science technology* **25**, 063001 (2012).
3. Eisaman, M. D., Fan, J., Migdall, A. & Polyakov, S. V. Invited review article: Single-photon sources and detectors. *Rev. scientific instruments* **82**, 071101 (2011).
4. Tang, Y.-L. *et al.* Measurement-device-independent quantum key distribution over 200 km. *Phys. review letters* **113**, 190501 (2014).
5. Yin, J. *et al.* Satellite-to-ground entanglement-based quantum key distribution. *Phys. review letters* **119**, 200501 (2017).
6. Liao, S.-K. *et al.* Satellite-to-ground quantum key distribution. *Nature* **549**, 43–47 (2017).
7. Wengerowsky, S. *et al.* Entanglement distribution over a 96-km-long submarine optical fiber. *Proc. Natl. Acad. Sci.* **116**, 6684–6688 (2019).
8. Zhong, H.-S. *et al.* 12-photon entanglement and scalable scattershot boson sampling with optimal entangled-photon pairs from parametric down-conversion. *Phys. review letters* **121**, 250505 (2018).
9. Wang, H. *et al.* Boson sampling with 20 input photons and a 60-mode interferometer in a 10¹⁴-dimensional hilbert space. *Phys. review letters* **123**, 250503 (2019).
10. Zhong, T. *et al.* Photon-efficient quantum key distribution using time–energy entanglement with high-dimensional encoding. *New J. Phys.* **17**, 022002 (2015).
11. Islam, N. T., Lim, C. C. W., Cahall, C., Kim, J. & Gauthier, D. J. Provably secure and high-rate quantum key distribution with time-bin qudits. *Sci. advances* **3**, e1701491 (2017).
12. Li, Z.-P. *et al.* Super-resolution single-photon imaging at 8.2 kilometers. *Opt. Express* **28**, 4076–4087 (2020).
13. McCarthy, A. *et al.* Kilometer-range, high resolution depth imaging via 1560 nm wavelength single-photon detection. *Opt. express* **21**, 8904–8915 (2013).
14. Hochberg, Y. *et al.* Detecting sub-gev dark matter with superconducting nanowires. *Phys. review letters* **123**, 151802 (2019).
15. Pe'er, A., Bromberg, Y., Dayan, B., Silberberg, Y. & Friesem, A. A. Broadband sum-frequency generation as an efficient two-photon detector for optical tomography. *Opt. Express* **15**, 8760–8769 (2007).
16. Wollman, E. E. *et al.* Kilopixel array of superconducting nanowire single-photon detectors. *Opt. express* **27**, 35279–35289 (2019).
17. De Greve, K. *et al.* Quantum-dot spin–photon entanglement via frequency downconversion to telecom wavelength. *Nature* **491**, 421–425 (2012).
18. Shalm, L. K. *et al.* Strong loophole-free test of local realism. *Phys. review letters* **115**, 250402 (2015).
19. Giustina, M. *et al.* Significant-loophole-free test of bell's theorem with entangled photons. *Phys. review letters* **115**, 250401 (2015).
20. Marsili, F. *et al.* Detecting single infrared photons with 93% system efficiency. *Nat. Photonics* **7**, 210–214 (2013).
21. Zhang, W. *et al.* Nbn superconducting nanowire single photon detector with efficiency over 90% at 1550 nm wavelength operational at compact cryocooler temperature. *Sci. China Physics, Mech. & Astron.* **60**, 120314 (2017).
22. Esmaeil Zadeh, I. *et al.* Single-photon detectors combining high efficiency, high detection rates, and ultra-high timing resolution. *Apl Photonics* **2**, 111301 (2017).
23. Reddy, D. V. *et al.* Exceeding 95% system efficiency within the telecom c-band in superconducting nanowire single photon detectors. In *CLEO: QELS_Fundamental Science*, FF1A–3 (Optical Society of America, 2019).

24. Reddy, D. V., Lita, A. E., Nam, S. W., Mirin, R. P. & Verma, V. B. Achieving 98% system efficiency at 1550 nm in superconducting nanowire single photon detectors. In *Conference on Coherence and Quantum Optics*, W2B-2 (Optical Society of America, 2019).
25. Hu, P. *et al.* Detecting single infrared photons toward optimal system detection efficiency. *arXiv preprint arXiv:2009.14690* (2020).
26. Miki, S. *et al.* Superconducting nbtin nanowire single photon detectors with low kinetic inductance. *Appl. physics express* **2**, 075002 (2009).
27. Yang, J. K. *et al.* Modeling the electrical and thermal response of superconducting nanowire single-photon detectors. *IEEE transactions on applied superconductivity* **17**, 581–585 (2007).
28. You, L. *et al.* Jitter analysis of a superconducting nanowire single photon detector. *Aip Adv.* **3**, 072135 (2013).
29. Li, H. *et al.* Multispectral superconducting nanowire single photon detector. *Opt. express* **27**, 4727–4733 (2019).
30. Zichi, J. *et al.* Optimizing the stoichiometry of ultrathin nbtin films for high-performance superconducting nanowire single-photon detectors. *Opt. Express* **27**, 26579–26587 (2019).
31. Miki, S., Yabuno, M., Yamashita, T. & Terai, H. Stable, high-performance operation of a fiber-coupled superconducting nanowire avalanche photon detector. *Opt. express* **25**, 6796–6804 (2017).
32. Dorenbos, S. *et al.* Superconducting single photon detectors with minimized polarization dependence. *Appl. Phys. Lett.* **93**, 161102 (2008).

Acknowledgements

J.C. acknowledges China Scholarships Council (CSC), No.201603170247. I.E.Z., V.Z., and Single Quantum B.V. acknowledge the supports from the ATTRACT project funded by the EC under Grant Agreement 777222. I.E.Z. acknowledges the support of Nederlandse Organisatie voor Wetenschappelijk Onderzoek (NWO), LIFT-HTSM (Project 680-91-202). R.B.M.G. acknowledges support by the European Commission via the Marie-Sklodowska Curie action Phonsi (H2020-MSCA-ITN-642656). V.Z. acknowledges funding from the Knut and Alice Wallenberg Foundation Grant “Quantum Sensors”, and support from the Swedish Research Council (VR) through the VR Grant for International Recruitment of Leading Researchers (Ref 2013-7152) and Research Environment Grant (Ref 2016-06122).

Competing interests

The authors declare no conflicts of interest.

Supplementary Material

Detecting Infrared Single Photons with Near-Unity System Detection Efficiency

Jin Chang^{1,2,*}, Johannes W. N. Los^{2,*}, Jaime Oscar Tenorio-Pearl², Niels Noordzij², Ronan Gourgues², Antonio Guardiani², Julien R. Zichi³, Sylvania F. Pereira¹, H. Paul Urbach¹, Val Zwiller³, Sander N. Dorenbos², and Iman Esmail Zadeh^{1,2}

¹Optics Research Group, ImPhys Department, Faculty of Applied Sciences, Delft University of Technology, Delft 2628 CJ, The Netherlands.

²Single Quantum B.V., Delft 2628 CJ, The Netherlands.

³Quantum Nano Photonics Group, Department of Applied Physics, Royal Institute of Technology (KTH), Stockholm 106 91, Sweden

*These authors contributed equally to this work.

Corresponding author: j.chang-1@tudelft.nl

Contents:

S1 List of measured devices

S1.1 Overview of tested detectors

S1.2 Detailed measurements of selected detectors

S2 Device Fabrication

S3 Optical Simulation

S4 Tunable laser source

S5 Optical power meters

S6 Efficiency measurement stability

S6.1 Optical attenuator stability

S6.2 Optical input power stability

S7 Measurement uncertainty

S8 Fiber end-face reflection

S8.1 Simulation of fiber end-face reflection

S8.2 Measurement of fiber end-face reflection

S9 Polarization degree and polarization control

S10 References

S1 List of measured devices

S1.1 Overview of tested detectors

Table S1.1 Overview of all measured detectors

Detector No.	Wavelength (nm)	SDE (%)	Jitter* (ps)	SDE uncertainty
1 ^a	1350	99.5	31 (RT)	± 2.07%
2	1280/1500	94	29 (RT)	± 2.07%
3	1425	98	26 (cryo)	± 2.07%
4	1350	95	32 (RT)	± 2.07%
5	1310	94	39 (RT)	± 2.07%
6 ^b	1550	83.3	18.7 (cryo)	± 5.9%
7	1550	80.5	24 (cryo)	± 5.9%
8	1550	83.3	35 (RT)	± 5.9%
9	1310	83.6		± 5.9%
10	1310	84		± 5.9%
11	1550	84		± 5.9%
12	1310	84.3		± 5.9%
13 ^c	1392	93.6	35.3 (RT)	± 5.9%
14	1550	85	31 (RT)	± 5.9%
15	1278	91.3	15.1 (cryo)	± 5.9%
16	1550	89	17.3 (cryo)	± 5.9%
17	1392	85	19.1 (cryo)	± 5.9%
18	1550	82	19.5 (cryo)	± 5.9%
19	1550	82.5	19 (cryo)	± 5.9%
20	1310	85.4		± 5.9%
21	1310	87		± 5.9%
22	1310	85		± 5.9%
23	1550	90.1		± 5.9%
24	1510	91.4		± 5.9%
25	1301	91		± 5.9%
26	1301	90.5		± 5.9%
27	1301	85		± 5.9%
28	1425	93.5		± 5.9%
29	1310	89.7		± 5.9%
30	1310	85.6		± 5.9%
31	1310	87.2		± 5.9%
32	1550	80		± 5.9%
33-40	Low efficiency or broken detectors, not registered here.			

* Jitter with ‘cryo’ label means measured with a cryogenic amplifier and jitter with ‘RT’ label means measured with a room-temperature amplifier.

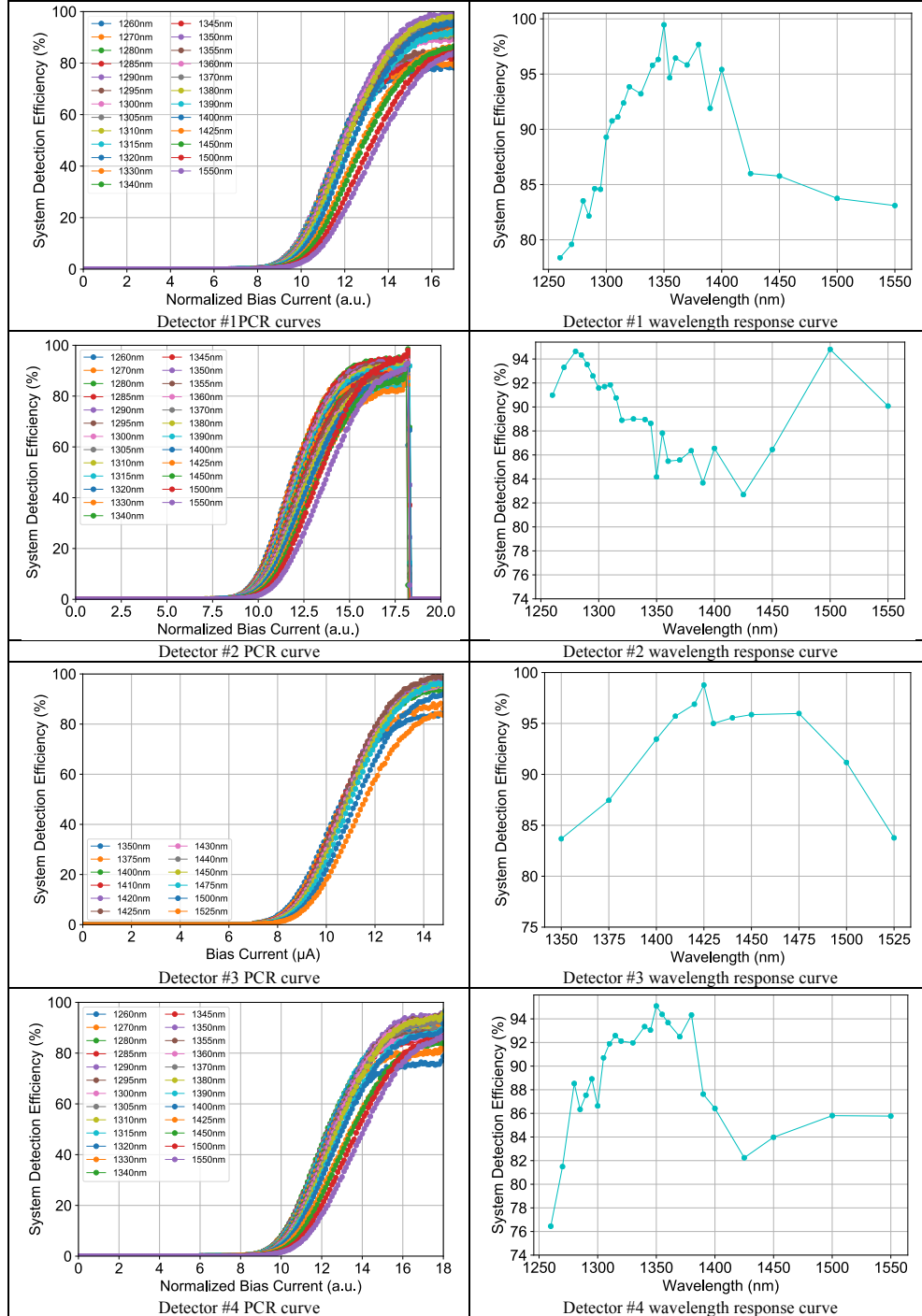
^a Detectors labelled with red fonts have efficiency > 90%. They were fully tested at multiple wavelengths.

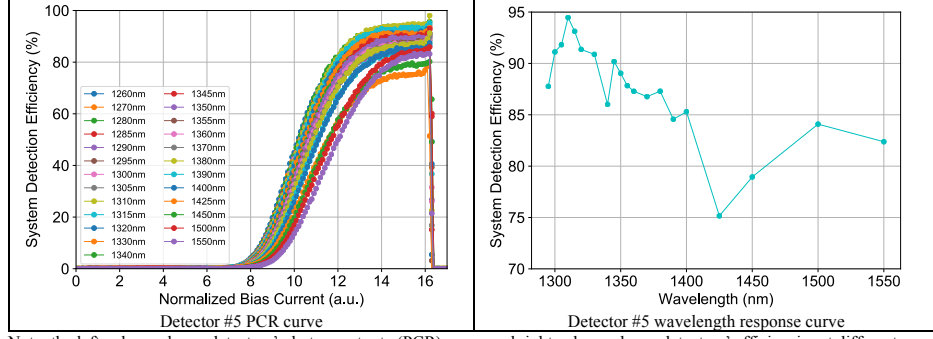
^b Detectors labelled with black fonts have efficiency < 85%. However, they were only tested at a few wavelengths. At other wavelengths they may reach higher efficiencies.

^c Detectors labelled with green fonts have efficiency > 85%. However, they were also only tested at a few certain wavelengths. At other wavelengths they may reach higher efficiencies.

S1.2 Detailed measurements of selected detectors

Table S1.2 Photocount rate curve and system efficiency measurement of selected detectors at different wavelengths





Note: the left column shows detectors' photocount rate (PCR) curve and right column shows detectors' efficiencies at different measured wavelengths. The system detection efficiencies have an uncertainty of $\pm 2.07\%$.

S2 Device Fabrication

We fabricated our detectors in the following order as shown in figure S2.1: Initially, a 230 nm thick SiO_2 layer was grown by thermal oxidation on a 4-inch Si wafer. On top of the SiO_2 , a NbTiN thin film was deposited by magnetron co-sputtering (Nb and Ti) deposition in a mixture of Argon and Nitrogen [1]. After that, the contact pads were formed using optical lithography, metal evaporation (Cr/Au, 5/55nm) and lift-off. Meandered nanowire structure was defined by electron beam lithography with either HSQ (1st batch, negative resist) or ARP-6200-4 (2nd batch, positive resist) E-beam resist. After development, the nanowire patterns were transferred to the NbTiN layer by reactive ion etching in a mixture of SF_6 and O_2 chemistry. Afterwards, EUV optical lithography was employed to open windows with a photo-resist (S1813) at the back side of the wafer, aligning it to the active area of the devices on the front side. After making the opening, a selective deep reactive ion etching (a Bosch process) was used to remove $\sim 280 \mu\text{m}$ Si before stopping at the SiO_2 layer. Cr/Au (2-3nm/150nm) was then deposited to form the mirror under SiO_2 membrane. Finally, a second Bosch etching recipe was used to release each individual detector.

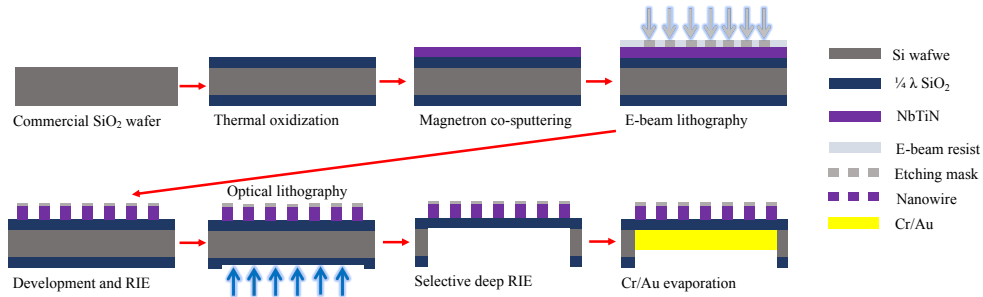


Figure S2.1 Device nanofabrication process

S3 Optical Simulation

We employed commercial software Lumerical for optical cavity simulation. To ensure accuracy, a mesh with a maximum mesh setting of 1/10 of the smallest feature size was applied around the meander. A power monitor was then placed over the meander layer to calculate light absorption. The absorption was then calculated as the net power flow into this monitor by normalizing to the total optical power. For the optical constants, the

following data was used. Since the thickness of Cr is much less than Au, and also Au diffuses into Cr layer, we take Au layer as reflector only in our simulation.

Fiber and $\frac{1}{4} \lambda$ layer:	SiO ₂ (Glass) – Palik.
Mirror:	Au (Gold) – CRC.
SNSPD meander:	NbTiN ellipsometry measurement of a film sputtered with the same recipe.

S4 Tunable laser source

In this work, we used a JGR-TLS5 tunable laser as light source for system efficiency measurements. As shown in the figure S4.1, we measured the laser spectrum with YOKOGAWA (AQ6374) optical spectrum analyzer. Figure S4.1. (a) shows the laser spectrum in the range of 1290-1650 nm; figure S4.1.(b) shows two measured wavelengths, 1340 and 1350 nm; and figure S4.1.(c) shows the laser spectrum at 1450 nm with FWHM linewidth of ~ 0.1 nm. In table S4.2, detailed optical specifications of the laser are listed.

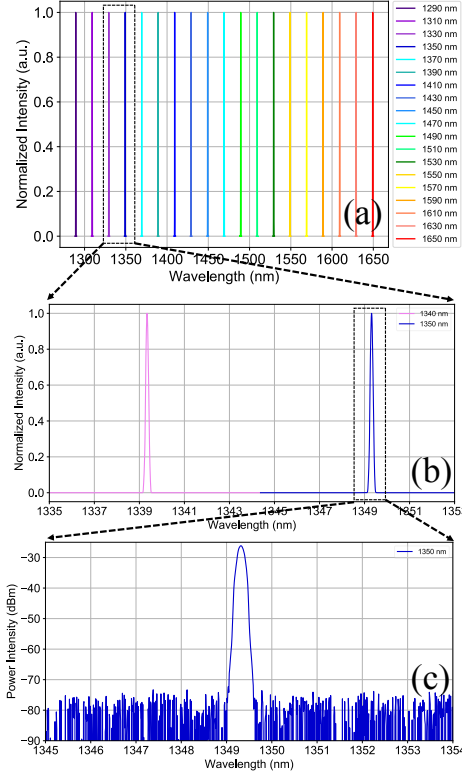


Figure S4.1.(a) Measured tunable laser spectrum at 1290-1650 nm, (b) measured laser spectrum at 1340 and 1350 nm, and (c) measured laser spectrum at 1350 nm.

Table S4.2 Optical specifications of the laser [2].

Parameter	Specification
Power stability	± 0.01 dB
FWHM linewidth	0.1 nm
Side Mode Suppression Ratio @0.1nm BW	>60 dB
Wavelength stability	± 50 pm
Resolution	0.1 nm
Operation temperature	0-40 °C
Wavelength range	1260-1650 nm
Humidity	Maximum 95% RH (0 to 40 °C)

S5 Optical power meters

Optical power meters can be used to measure CW laser power. In our work, we compared and measured the performance of three different types of semiconductor optical power meters. The details are shown in table S5.1. In our SDE measurement, we employed the Newport 818-IG-L (InGaAs) power meter for setting up the optical power attenuation ratio (for example, $P_1/P_2=50\text{dB}$, see figure S6.1) as well as measuring the optical power at the reference port (P_1 , see figure S6.1). The main reason for using Newport 818-IG-L power meter is because of high linearity ($\pm 0.5\%$), good accuracy ($\pm 2\%$) and of prime importance its high input dynamic range (20 pW-10 mW).

Table S5.1 Performance of different types of semiconductor optical power meters.

Power meter	Thorlabs S154C (InGaAs)	Newport 818-IG-L (InGaAs)	Newport 918D OD3R (Germanium)
Specification			
Serial Number	190906316/ 190906317	N-12680	1659
Wavelength range	800-1700 nm	800-1650 nm	780-1800 nm
Optical power working range	100 pW-3 mW	20 pW-10 mW	5 nW-2 mW
Linearity	$\pm 0.5\%$	$\pm 0.5\%$	$\pm 2\%$ @ 911-1700 nm
Measurement Uncertainty	$\pm 5\%$	$\pm 2\%$	$\pm 2\%$

S6 Efficiency measurement stability

S6.1 Optical attenuator stability

As shown in figure S6.1 (also described in the main text, see section ‘Efficiency Measurement Setup’), the optical attenuator is built by setting up the power ratio $P_1/P_2 = (50-60)$ dB. We measure the power P_1 and P_2 with Newport 818-IG-L power meter before and after SDE measurements as shown in table S6.2. As a result, the attenuation ratio before and after SDE is maintained at 50dB with an uncertainty of $< 0.2\%$.

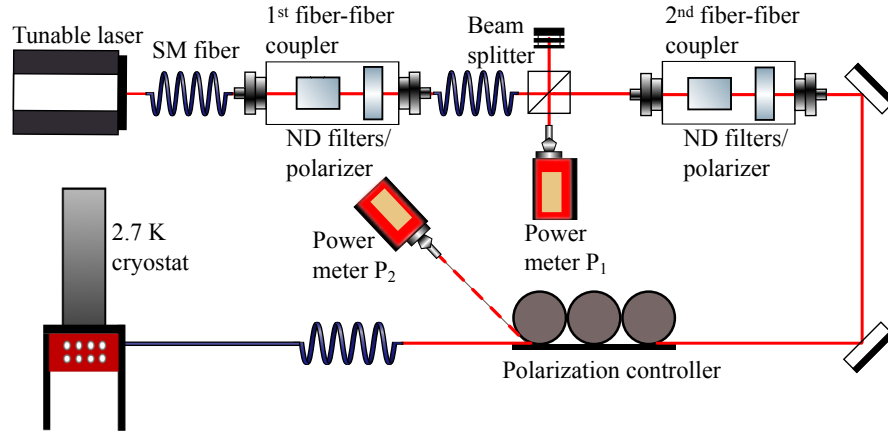


Figure S6.1 System detection efficiency measurement setup.

Table S6.2 Typical power meter readings before and after SDE measurement.

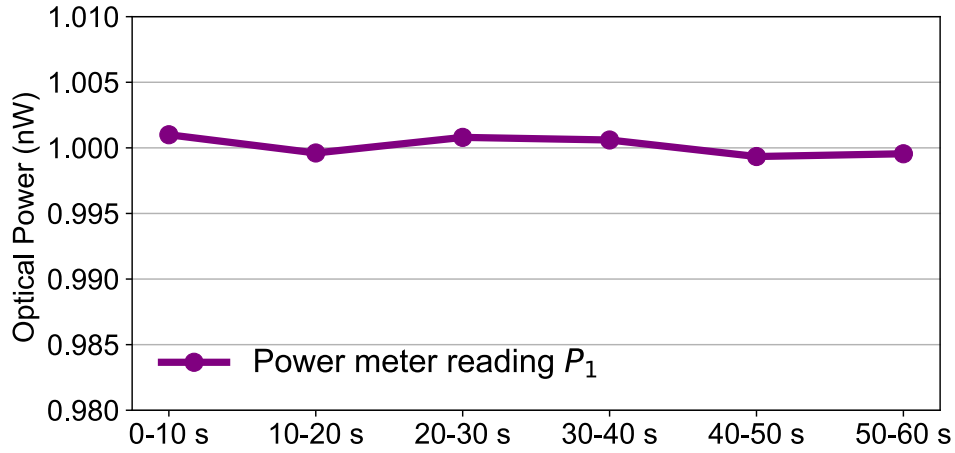
Powers meters Recorded values	Power meter P_1 (before SDE measurement)	Power meter P_2 (before SDE measurement)	Power meter P_1 (after SDE measurement)	Power meter P_2 (after SDE measurement)
Mean power	358.79 μW	3.59 nW	358.54 μW	3.59 nW
Attenuation ration	50 dB		50 dB	

S6.2 Optical input power stability

Since our SDE measurement setup has two ports: reference port (power meter P_1) and measurement port (power meter P_2), it allows us to monitor the input photon flux in real time during SDE measurement by reading power meter P_1 . For example, after setting the attenuation ratio $P_1/P_2=50$ dB, we add neutral density filters in the first fiber-fiber coupler before the polarizer to make $P_1=1$ nW. Then we start SDE measurement and at the same time, we record the readings from power meter P_1 constantly. Table S6.3 and figure S6.4 show the reading from power meter P_1 during one of our SDE measurement and the input photon flux uncertainty is $< 0.1\%$.

Table S6.3 Optical power P_1 reading during one SDE measurement

Time	0-10 s	10-20 s	20-30 s	30-40s	40-50 s	50-60 s
Power P_1 (nW)	1.001	0.99961	1.0008	1.0006	0.99934	0.99955

Figure S6.4 Optical power P_1 reading during SDE measurement.

S7 Measurement uncertainty

For SDE measurement uncertainty, we considered all possible uncertainties in our experiments and then calculated the total measurement uncertainty with the root-mean-square (RMS) of the sum of the squared errors [3]. The uncertainties in our measurements include the power meter uncertainty ($\sigma_1=2\%$) and its linearity uncertainty ($\sigma_2=0.5\%$), laser stability uncertainty ($\sigma_3<0.1\%$) and optical attenuator uncertainty ($\sigma_4<0.2\%$). Our efficiency measurement has a total uncertainty of $\sqrt{\sigma_1^2 + \sigma_2^2 + \sigma_3^2 + \sigma_4^2} = 2.07\%$.

S8 Fiber end-face reflection

S8.1 Simulation of fiber end-face reflection

As discussed in the main text (see section ‘Fiber end-face reflection’), when measuring the laser power within the fiber with a power meter, the fiber end-facet is not in direct contact with the power meter’s sensor. The existing fiber-to-air interface causes reflection, back towards the light source. On the other hand, physical contact polished fiber to fiber connections (when connecting the same fiber to the system input fiber) have negligible back reflections (typically -30 to -40 dB). Thus, for all our efficiency measurements, we removed this back-reflection contribution by multiplying a correction factor of $(1-R_{\eta})$ [4]. Below we show FDTD simulation results of the fiber end-face reflection at different wavelengths. In short, we built the optical fiber structure (core radius $4.1\ \mu\text{m}$, refractive index 1.45625/cladding radius $62.5\ \mu\text{m}$, refractive index 1.45282) and then put a Gaussian mode source inside the fiber. A monitor was placed at the back side of the mode source and collected the reflected light from the fiber end-face and air interface. As shown in figure S8.1, the reflection R_{η} is in the range of 3.41-3.43% from 1300-1550 nm.

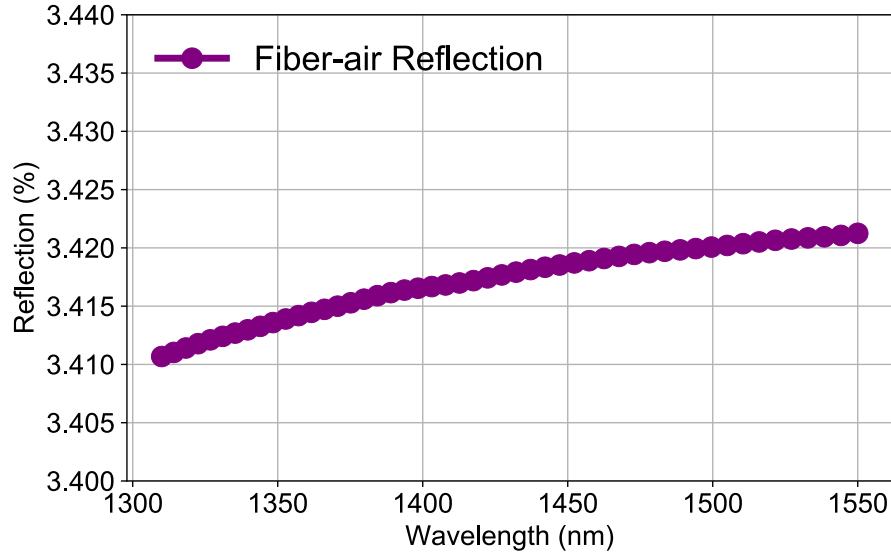
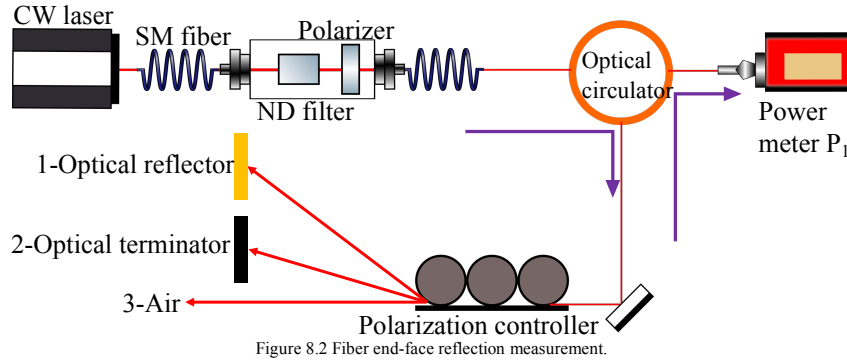


Figure S8.1 Simulated fiber end-face reflection at different wavelengths.

S8.2 Measurement of fiber end-face reflection

Besides FDTD simulation, we also experimentally measured the fiber end face reflection. Figure S8.2 shows how we experimentally acquire the value of R_{ref} . Light from the tunable laser source pass through the free space fiber-fiber coupler (containing neutral density filter and polarizer) and goes to an optical circulator. Then light is directed to a polarization controller (PC) and at the end of the PC, the fiber is connected to either an optical reflector (connection 1), or an optical terminator (connection 2) or towards air (connection 3). The reflected light from the end of the PC is guided by the optical circulator to an optical power meter P_1 and its power is recorded. The recorded reflection power from the above mentioned 3 different connections are recorded as P_{Ref} , P_{Ter} and P_{Air} . Based on these values, we acquired the fiber end face reflection value $R_{ref} = \frac{P_{Air} - P_{Ter}}{P_{Ref}}$. We acquired a R_{ref} in the range of (3.4-3.6) % thus for our efficiency measurement, we considered a conservative correction factor of $R_{ref} = 3.6\%$.



S9 Polarization degree and polarization control

Since our detectors are patterned into meandering shapes, light absorption can be significantly different based on the light polarization direction [5]. Thus, it is important to have a linearly polarized input light and fully control the polarization. In figure S9.1, we show the measurement of light polarization before connecting to the system for SDE measurement (set up is shown in figure S6.1) with a polarimeter (Thorlabs-PAX1000IR2/M). As shown from figure S9.1. (a) to S9.1. (f), by turning the polarization controller, we can fully control the polarization of the light. More importantly, in S9.1. (f) we show that the light has a degree of polarization of $\sim 100\%$ ($\pm 0.09\%$), a degree of linear polarization of 99.97%. It indicates that the light is linearly polarized and its polarization can be fully controller by the polarization controller, which is important to reach near-unity SDE.

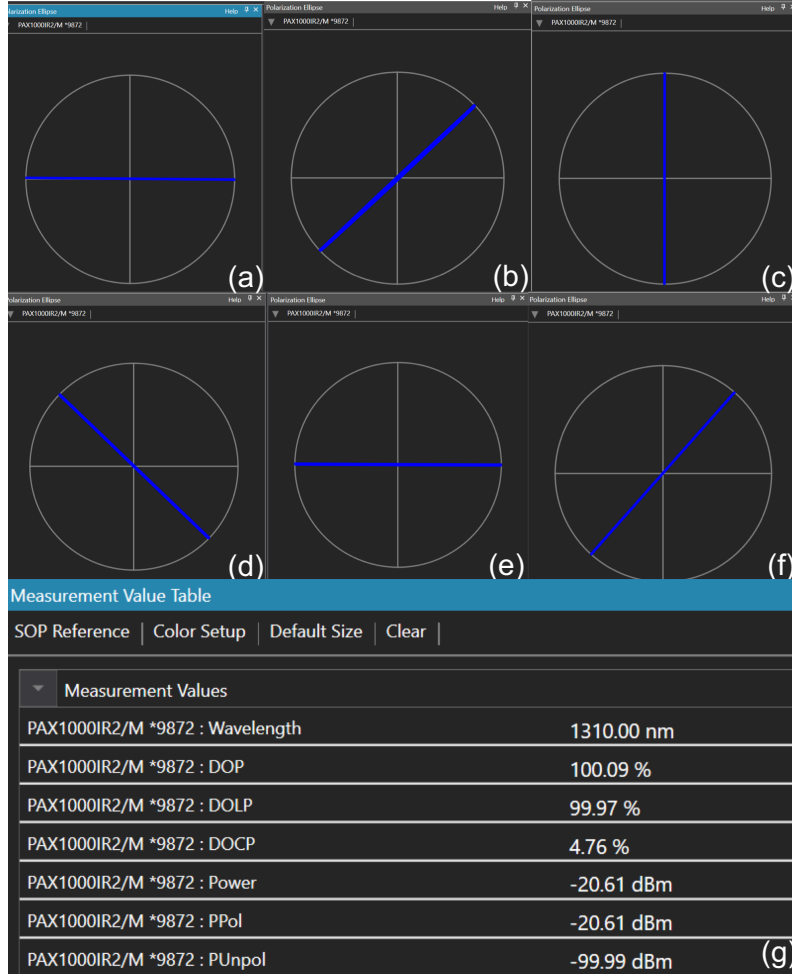


Figure 9.1 (a)-(f) show fully control of light polarization and (g) shows that light for our SDE measurement is ~100% linearly polarized.

S10 References:

- [1] Zichi, J. *et al.* Optimizing the stoichiometry of ultrathin NbTiN films for high-performance superconducting nanowire single-photon detectors. *Opt. Express* 27, 26579–26587 (2019).
- [2] <https://jgroptics.com/uploads/files/TLS5-Spec-Sheet-1020.pdf>
- [3] Marsili, F. *et al.* Detecting single infrared photons with 93% system efficiency. *Nat. Photonics* 7, 210–214 (2013).
- [4] Esmaeil Zadeh, I. *et al.* Single-photon detectors combining high efficiency, high detection rates, and ultra-high timing resolution. *Apl Photonics* 2, 111301 (2017).
- [5] Dorenbos, S. *et al.* Superconducting single photon detectors with minimized polarization dependence. *Appl. Phys. Lett.* 93, 233161102 (2008).